Article | Received 24 February 2026; Revised 28 May 2026; Accepted 2 June 2026; Published 30 June 2026
https://doi.org/10.55092/aimat20260008

Machine learning-based ion sieve forming strategy: impact on salt lake lithium recovery by fixed beds

Jiangtao Yu[1,*], Zegang Fu[1], Pakiza Ajibek[1], Meng Zhang[2], Weihua Hong[1] and Feng Gao[1,*]

[1] Key Laboratory of Chemical Engineering in South Xinjiang, College of Chemistry and Chemical Engineering, Tarim University, Alar 843300, China
[2] State Key Laboratory of Heavy Oil Processing, College of Chemical Engineering and Environment, China University of Petroleum-Beijing, Beijing 102249, China

* Correspondence authors; E-mails: 120250077@taru.edu.cn (J.Y.); gaofeng137@tju.edu.cn (F.G.).

Highlights:

- For the first time, AI was applied to analyze the shaping strategy of fixed-bed adsorbents for lithium extraction from salt lakes, and a multi-model analysis framework was established.
- It was confirmed that the efficiency of liquid film mass transfer has a much greater impact on the performance of the fixed bed than the adsorbent material itself.
- The optimal structural parameters of the fixed bed filler were selected, and it was clarified that the design of the filler structure is the core for optimization.

Abstract: Lithium recovery from salt-lake brines is of great significance for addressing the growing demand for lithium resources. Fixed-bed adsorption is a key process in lithium recovery from salt lakes, and the shaping strategy of the adsorbent plays a decisive role in determining fixed-bed performance. This study is the first to apply machine learning to analyze the shaping strategy of fixed-bed adsorbents for lithium recovery from salt lakes. A multi-model analytical framework integrating back propagation (BP), radial basis function (RBF), probabilistic neural network (PNN), generalized regression neural network (GRNN), random forest (RF), and genetic algorithm (GA) models was established to evaluate the effects of material properties, process parameters, and shaping strategies on fixed-bed adsorption performance. The results showed that the liquid-film mass transfer efficiency has a greater influence on fixed-bed performance than the adsorbent material itself. The optimal structural parameters were identified using the radial basis function–genetic algorithm (RBF-GA) model and further validated experimentally by response surface methodology (RSM). The optimized conditions were determined to be a packing diameter of 12.5 mm and a packing density of 0.30. This work provides new insight into the structural design of fixed-bed adsorbents and offers a useful reference for the development and optimization of lithium recovery processes from salt-lake brines.

Keywords: lithium recovery; lithium-ion sieve; dynamic adsorption; fixed-bed packing; artificial neural networks

1. Introduction

Lithium is a critical resource with extensive applications in metallurgy [1], ceramics [2], and other fields [3]. In recent years, the rapid growth of the lithium battery industry has dramatically increased global demand for lithium, raising concerns that terrestrial lithium reserves may be insufficient to meet future requirements [4]. At present, approximately 66% of the world's lithium is contained in salt-lake brines [5]. To recover lithium from salt lakes, several technologies have been developed, including electrochemical methods [6], recovery [7], adsorption [8] and precipitation [9]. Among these, adsorption has emerged as one of the most promising techniques due to its operational simplicity, high efficiency, and excellent selectivity [10–12]. In particular, titanium-based lithium-ion sieves have been widely investigated for lithium recovery from brines due to their low solubility loss and stable performance [13], making them a pivotal material for sustainable lithium recovery and utilization [14,15].

The recovery of lithium from salt-lake brines using titanium-based lithium-ion sieves (Ti-LIS) is commonly carried out in fixed-bed reactors, which serve as the main unit for the adsorption process [16,17]. In this context, the design of the adsorbent is a key factor governing recovery efficiency [15,18]. At present, the mainstream approach to improving the adsorption performance of lithium-ion sieves is element doping. For instance, Zhao *et al.* prepared a Co-doped Li_2TiO_3 using the calcination method. Compared to the traditional Li_2TiO_3, the adsorption capacity of this ion sieve increased by 1.4 times, and it also exhibited excellent cycling performance [19]. However, the products prepared by these methods are mostly in powder form and cannot be directly applied in the fixed-bed adsorption process. Therefore, selecting an appropriate forming process is the key to using lithium-ion sieves in the fixed-bed process [20,21].

The adsorbent forming process is crucial for addressing the high pressure of powder in the fixed bed and the loss of powder [22,23]. The common powder forming processes include granulation, extrusion forming, electrospinning, and 3D printing [24–26]. How to select the appropriate forming strategy has always been the key to the research in the fixed bed process. For example, Ren *et al.* prepared an Heterogeneous Metal Oxide/M-Xene/Polysulfone (HMO/MXene/PSF) adsorption membrane. This author utilized two-dimensional MXene to connect H and other components. The experimental results showed that the membrane prepared by this method had significant cycle stability [27]. Besides preparing the membrane, there are also studies that have prepared lithium-ion sieves into granular adsorbents, such as Zhao *et al.* used Polyvinyl chloride (PVC) as a binder to prepare granular adsorbents and studied the influence of the binder on the adsorption process. The results showed that polyacrylic acid as a binder can help the ion sieve achieve better dispersion and exhibit good hydrophilicity and good binder compatibility properties [28]. Furthermore, in our previous research, we also attempted to use montmorillonite as a binder to prepare 3D-printed monolithic adsorbents with high compressive strength and regular channels. The experimental results showed that the compressive strength of the 3D-printed monolithic adsorbents could reach 51 MPa, and the adsorption capacity could reach 80% of the powder [29]. It can be observed that the current methods for forming the adsorption system for lithium recovery mainly include granulation, 3D printing, and electrospinning. However, due to the significant differences among these forming strategies, and each forming process having its own advantages and disadvantages, it is impossible to conduct a comprehensive comparison of each one and

optimize the best fixed-bed packing structure [30,31]. Therefore, choosing the appropriate forming method is the key to achieving efficient adsorption in the fixed bed [32,33].

Machine learning, due to its outstanding nonlinear optimization capabilities, is widely applied in fields such as image recognition, process prediction, and nonlinear modeling [34,35]. Syu *et al.* regarded Artificial Neural Network (ANN) as a new computational method and first applied it to the modeling of seven multi-component adsorption systems. This research successfully utilized the backpropagation neural network model with saturation transfer functions. The results showed that the adsorption isotherms generated by the ANN model had a significantly better correlation with the experimental data compared to the results of the multi-component Langmuir model [36]. Furthermore, Raccuglia *et al.* explored how to utilize machine learning algorithms to predict the process of synthesizing vanadium-selenium compounds using crystallization templates. This study collected data from failed hydrothermal synthesis experiments conducted in their laboratory and combined with chemoinformatic, added physical and chemical property descriptions to the original information. Based on these data, this work successfully trained a machine learning model for predicting the success rate of the reaction. The author reversed the machine learning model, and this work also proposed new hypotheses regarding the material formation conditions [37]. Therefore, it is feasible to conduct an analysis and study on the forming strategy of the adsorbent in the fixed bed through machine learning [38,39].

This study is the first to propose the use of machine learning to analyze and compare the influence of the forming process on the fixed-bed process during the lithium adsorption recovery process. Firstly, this work established back propagation (BP) and radial basis function (RBF) neural networks with high prediction accuracy based on the data collected from the literature. Subsequently, the importance of the influencing factors of the fixed-bed was analyzed using the random forest (RF) algorithm. Finally, the optimal fixed-bed structure was selected through the radial basis function-genetic algorithm (RBF-GA) model. In addition, the results of the machine learning model were verified through experimental data combined with the response surface method. It can be found that in the fixed-bed process, the structural parameters during the forming process > the process parameters of the fixed-bed adsorption > the factors of the material itself. The results are similar to the conclusions obtained from the experimental verification using the response surface method. Therefore, we can conclude that in the fixed-bed process of lithium adsorption recovery, the liquid film mass transfer efficiency has a much greater impact on the performance of the fixed bed than the material itself on the lithium-ion adsorption process. This provides guidance for the subsequent design of the fixed-bed structure and the optimization of the forming method.

2. Experimental

2.1. Material

Titanium dioxide(A.R.), Lithium carbonate(A.R.), Lithium hydroxide monohydrate ($LiOH \cdot H_2O$, ≥ 95.0%), hydrochloric acid (HCl), was obtained from Sinopharm Chemical Reagent Co., Ltd. Montmorillonite was purchased from Shijiazhuang Natural Collection Co., Ltd. Real brine was obtained from Lake Zabye form Jiangsu Tefeng Co., Ltd.

2.2. Preparation of 3D-printed monolithic adsorbent

The preparation method of lithium titanate particles is as follows: (1) Weigh lithium carbonate and titanium dioxide in a 1:1 molar ratio; (2) Disperse and stir the above mixed powder in anhydrous ethanol for 4 hours and then dry it; (3) Place the mixed powder in a muffle furnace and heat it at a temperature increase rate of 5 °C/min to 650 °C for 4 hours.

Preparation of 3D printing slurry: (1) Weigh lithium titanate particles and montmorillonite in a mass ratio of 8:2; (2) Add deionized water according to the mass ratio of montmorillonite and deionized water as 1:5, and continuously stir to obtain a uniform slurry; (3) Seal and store the mixed prepared slurry for the subsequent printing process.

3D printing of monolithic adsorbent process: (1) Model the structure in C4D according to the selected structure; (2) Convert the designed model into G code in the slicing software; (3) Use the direct writing 3D printer to shape the prepared monolithic adsorbent.

2.3. Construction of backpropagation artificial neural network

In this paper, MATLAB 2021b is used to develop the network architecture and optimize the parameters. In this work, an artificial neural network is designed using BP algorithm. To reduce errors, all variables are normalized to a range of 0 to 1. The normalization process is as follows:

$$Y_{i,norm}=\frac{Y_i - Y_{i,min}}{Y_{i,max} - Y_{i,min}} \quad (1)$$

In the formula, $Y_{i,\,min}$, and $Y_{i,\,max}$ represent the minimum and maximum values of the variable Y respectively.

2.3.1. Construction of radial basis artificial neural network

The structure of RBF artificial neural network model and BP artificial neural network model is composed of input layer, hidden layer and output layer. The biggest difference between RBF artificial neural network and BP neural network is that the data transmission process of RBF neural network only has one-way transmission of data, and there is no backpropagation of error. Therefore, compared with BP artificial neural network, the training speed of RBF neural network is faster. The overall structure of RBF artificial neural network is as follows:

$$y(x) = W\Phi(x) + b \quad (2)$$

In this formula, $y(x) = [y_1(x), y_1(x),\ldots,y_k(x)]^T$ is the output vector, in this work, the output vector is the ratio of the concentration at the outlet of the fixed bed to the concentration at the entrance outlet-to-inlet concentration ratio (C_t/C_0).W is the weight matrix, representing the set of connection weights w_{kj} between each neuron, the size of which is determined by the training process of RBF artificial neural network.$\Phi(x) = [\varphi_1(x), \varphi_2(x),\ldots,y_m(x)]^T$ is the input vector of the radial basis function, which represents the characteristics of the input parameters.The input vectors of this work mainly include printing type, Langmmuir adsorption constant and inlet concentration. $B = [b_1, b_1,\ldots, b_k]^T$ is a bias vector used in RBF artificial neural networks for data adjustment to increase the computational accuracy of the model.

The biggest difference between RBF artificial neural networks and BP artificial neural networks is that each neuron uses a different function. RBF artificial neural network uses Gaussian function as radial basis function, the formula is as follows:

$$\phi_j(x) = e^{\left(-\frac{\|x-c_j\|^2}{2\delta_j^2}\right)} \tag{3}$$

In this formula, C_j represents the center vector of the hidden layer neuron, and σ represents the width of the JTH hidden layer neuron. $||x-c_j||$ represents the euclidean distance between the input vector x and the center vector c_j.

2.4. Construction of probabilistic neural network and generalized regression neural network

Probabilistic neural network (PNN) and generalized regression neural network (GRNN) are special cases of RBF neural networks, which have attracted much attention because of their fast training process and good generalization ability. Both networks are suitable for classification and regression tasks. In this work, the type of fixed bed is predicted by PNN and GRNN.

The structure of PNN artificial neural network is mainly composed of the following parts: (1) Input layer: the input data is transmitted to the mode layer, and no data is processed in this process; (2) Pattern layer: each neuron represents a sample in the training data set and calculates the distance between the input vector and that sample. Gaussian radial basis function is usually used; (3) Summary layer: classify the output of the pattern layer and calculate the probability of each category; (4) Output layer: select the category with the greatest probability as the final classification result.

In the summary layer, the probability of each class is estimated as:

$$P(c_j|x) = \frac{1}{N_j}\sum_{i\in c_j}\phi_i(x) \tag{4}$$

In this formula, x is the input vector, N is the number of samples in the training dataset, xi is each sample, c_j represents the class of each sample, and N_j is the number of samples in class c_j. $\phi_i(x)$ is the parameter obtained from the input function by transforming the radial basis function. In the output layer, by comparing the probability of the data in the summary layer, the category with the greatest probability is selected as the final result:

$$c = \text{argmax}\left[P(c_j|x)\right] \tag{5}$$

In the formula, c is the category with the greatest probability after the comparison of probabilistic neural networks.

2.5. The construction of genetic algorithm

Genetic algorithm (GA) is a kind of optimization algorithm that simulates the process of biological evolution, and gradually finds the optimal individual in the solution space through selection, crossover and mutation. GA is especially suitable for complex, multidimensional, nonlinear and discontinuous optimization problems.

The basic structure of GA is mainly composed of the following parts: (1) Coding: used to represent individuals. The commonly used coding methods include binary coding, real coding, permutation

coding, *etc.* (2) Population initialization: generating initial populations, usually randomly; (3) Fitness function: used to evaluate the degree of an individual, that is, the fitness of an individual in the solution space; (4) Selection: select individuals according to fitness for generating the next generation of individuals. The commonly used methods include roulette choice, tournament choice, *etc.* (5) Crossover: the mating process of simulated organisms is mainly used to generate new individuals. Common methods include single-point crossover, multi-point crossover, uniform crossover, *etc.* (6) Variation: simulate the mutation process of organisms, and increase the diversity of populations by randomly modifying some genes of individuals. The commonly used methods include variation, exchange, *etc.* (7) Termination conditions: the stopping criteria of the algorithm. Common termination conditions include reaching the maximum number of iterations, fitness reaching the expected value, and population diversity below a certain threshold.

In the GA in this work, the fitness function is mainly used to evaluate the quality of the solution, and the prediction result of RBF artificial neural network is mainly used as the fitness function. Roulette is played to determine which individuals will be selected to participate in the process of generating the next generation. The goal of the roulette selection function is to select individuals based on their fitness values, thus ensuring that individuals with higher fitness have a greater chance of passing on their genes to the next generation.

$$\mathrm{pi} = \frac{\mathrm{f}(x_\mathrm{i})}{\sum_{\mathrm{j=i}}^{\mathrm{N}} \mathrm{f}(x_\mathrm{j})} \tag{6}$$

In this formula, the probability of each individual being selected is proportional to the fitness, and the fitness value of each individual is converted into a selection probability, by selecting an individual in a manner similar to spinning a roulette wheel. Where pi is the selection probability of individual x_i, f (x_i) is fitness, and N is population size.

2.6. Construction of response surface method

Response surface method is to optimize the performance of a process or system by designing experiments, building mathematical models, fitting response surfaces and finding the best combination of parameters. The core idea of response surface method is to establish the mathematical relationship between the input variable and the output response through the experimental data, and use the relationship to optimize. The method usually uses a polynomial model to approximate the relationship between the input variable and the output response, and the equation is as follows:

$$\mathrm{Y} = \mathrm{b}_0 + \sum_{\mathrm{i=1}}^{4} \mathrm{b}_\mathrm{i} x_\mathrm{i} + \sum_{\mathrm{i=1}}^{3} \sum_{\mathrm{j=i+1}}^{4} \mathrm{b}_\mathrm{ij}\, x_\mathrm{i} x_\mathrm{j} + \sum_{\mathrm{i=1}}^{4} \mathrm{b}_\mathrm{ii} x_\mathrm{i}^2 \tag{7}$$

In this formula, Y is the predicted response, x_i and x_j are independent variables, b_0 is the migration constant, b_i is the i th linear coefficient, b_{ii} is the quadratic coefficient, and b_{ij} is the interaction coefficient. In this work, Analysis of Variance (ANOVA) is also used to verify the fit degree of the accuracy of the model. The underlying principle of ANOVA is to compare variability between and within groups to determine if there are significant differences in the mean values of each group.

2.7. Source of parameter constraints

The upper and lower limits of the filler diameter, bulk density, printing needle diameter, and adsorption time all come from the actual operational range of the 3D direct writing device: fixed bed experimental conditions and the published work of our team [29]. Practical feasibility: Filler diameter 12.5 mm: This diameter is determined by the diameter of the fixed bed equipment we selected, and it matches the inner diameter of a conventional fixed bed adsorption column, with uniform fluid distribution and easy filling; the filling density is 0.3, and the upper limit of this value is due to if the filling density is higher than 0.3, during the printing process, due to the mutual accumulation of the extruded filler, the pores will be completely blocked. Needle diameter: 0.13 mm. The selection of this needle diameter is because the maximum needle diameter of the 3D printer is 0.13 mm. Adsorption time 190 min. The selection of this data is because in previous studies, it is generally around 3 hours that the adsorption equilibrium is reached, so this data is chosen as the maximum value, which is close to the dynamic adsorption equilibrium time of the titanium-based ion sieve in real salt lake brine, and is highly practical for engineering. Relevant literature and experimental conditions have been cited in the text to support the rationality of parameter selection.

2.8. Stability and cyclic performance tests

To evaluate the durability of the monolithic adsorbent under strongly acidic and alkaline conditions, 1 g of the monolithic adsorbent was immersed in 0.1 mol/L HCl solution and subjected to shaking in a water bath at 140 rpm for 12 h. Afterward, the mass of the adsorbent was measured. The same sample was then transferred into 0.1 mol/L LiOH solution and shaken again under the same conditions for another 12 h, followed by mass measurement. This procedure was repeated to simulate the long-term durability of the monolithic adsorbent under alternating strong acid and strong base environments.

For the cyclic performance test, 1 g of the monolithic adsorbent was placed in 0.1 mol/L HCl solution and shaken in a water bath at 70 rpm for 12 h to complete acid washing. The acid-washed adsorbent was then transferred into 200 ppm LiCl solution for lithium adsorption. After each adsorption cycle, the adsorption capacity was determined. This adsorption–desorption process was repeated for five cycles to evaluate the cyclic performance of the monolithic adsorbent.

2.9. Encoding section

In this work, the Langmuir adsorption constant was used as an input variable to represent the aqueous environment in the machine learning model. The rationale is that the adsorption process is affected by numerous factors. Specifically, the rate-controlling steps may involve multiple mass-transfer and diffusion phenomena, including fluid diffusion in the solution, liquid-film diffusion, intraparticle diffusion within the adsorbent, resistance at the adsorption sites, outward diffusion from the adsorbent, external film diffusion, and diffusion in the bulk solution. These resistances vary under different aqueous conditions and jointly influence the final adsorption performance, yet they are difficult to quantify individually. Therefore, using only variables such as ion concentration in solution and adsorbent type is insufficient to fully describe the diffusion behavior during adsorption.

Based on this consideration, we employed the Langmuir adsorption constant obtained from static adsorption experiments as a descriptor variable, and used dynamic adsorption data as the output for model training. This strategy is particularly meaningful because static adsorption experiments are often considerably more time-consuming and costly than dynamic adsorption tests. Accordingly, the main objective of this work is to establish a predictive framework in which dynamic adsorption behavior can be estimated directly from static adsorption results, thereby reducing the experimental burden associated with dynamic evaluation.

3. Results and discussion

3.1. Material characterization

3.1.1. Analysis of SEM

This work mainly uses lithium titanate as the adsorbent and montmorillonite as the binder to prepare granular adsorbents and 3D-printed monolithic adsorbents. The Figure 1a,d are the optical photos and scanning electron microscope (SEM) images of the synthesized lithium titanate, and it can be found that the lithium titanate prepared by this method has a good spherical structure, which is similar to the structure reported in the literature [29]. Figure 1b,e are the adsorbents after extrusion forming, and it can be found that montmorillonite, as a clay-type adsorbent, can well bond the titanium titanate particles together, and the good layered structure of montmorillonite can prevent the adsorption sites of titanium titanate particles from being completely blocked. Figure 1b,e are the monolithic adsorbents formed by 3D printing, and it can be found that this adsorbent has an ordered pore structure. It can be seen from the SEM images that the adsorbent prepared by this method can maintain a good pore structure at a smaller scale. It can be observed as shown in Figure 1c that this adsorbent has an ordered macroscopic structure. Moreover, as shown in Figure 1f, the SEM image indicates that montmorillonite has a microscopic sheet-like structure and will not block the transmission path of Li, thereby achieving a relatively fast mass transfer rate. Additionally, we have added the relevant schematic diagrams during the modeling process (Figure S1), in which it can be found that the structure during the modeling is an ordered porous structure, and the overall adsorbent printed by 3D printing is also an ordered porous structure. Furthermore, through computational fluid dynamics (CFD), it has been proved that this porous structure has good fluid mechanical properties.

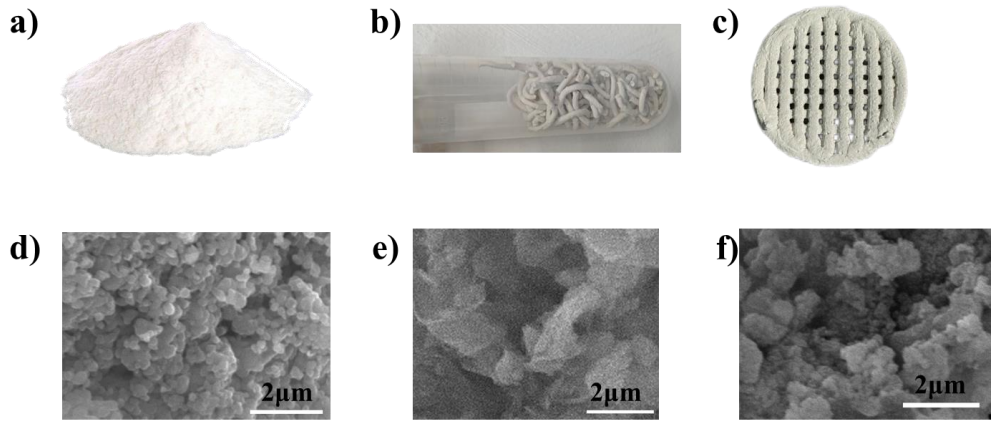

Figure 1. Optical photograph: **(a)** Lithium titanate powder; **(b)** Long strip-shaped adsorbent squeezed out by a needle; **(c)** 3D-printed integrated adsorption; SEM image; **(d)** Lithium titanate powder; **(e)** Long strip-shaped adsorbent; **(f)** 3D-printed integrated adsorption.

3.1.2. Analysis of XRD

In addition, this study also analyzed the crystal structure of the lithium titanate adsorbent before and after formation. The X-Ray Diffraction (XRD) results are shown in Figure 2. It can be observed that by simple calcination, lithium titanate particles with good crystal form can be formed. The main reason for this is that ethanol has a smaller polarity compared to water. When titanium dioxide and lithium carbonate powder are stirred in ethanol, better dispersion can be achieved, leading to better mixing. Moreover, by comparing the XRD pattern of the slurry and lithium titanate, it can be found that the characteristic diffraction of lithium titanate is clearly reflected in the slurry spectrum, and the peak positions are completely consistent with the standard card and pure lithium titanate samples. This fully demonstrates that the crystal phase structure of lithium titanate in the slurry has not changed due to the slurry preparation process. Through the analysis of the montmorillonite phase, it can be found that the characteristic peaks of montmorillonite in the formed slurry are relatively low, indicating that the content of montmorillonite in the slurry is relatively low in this formulation.

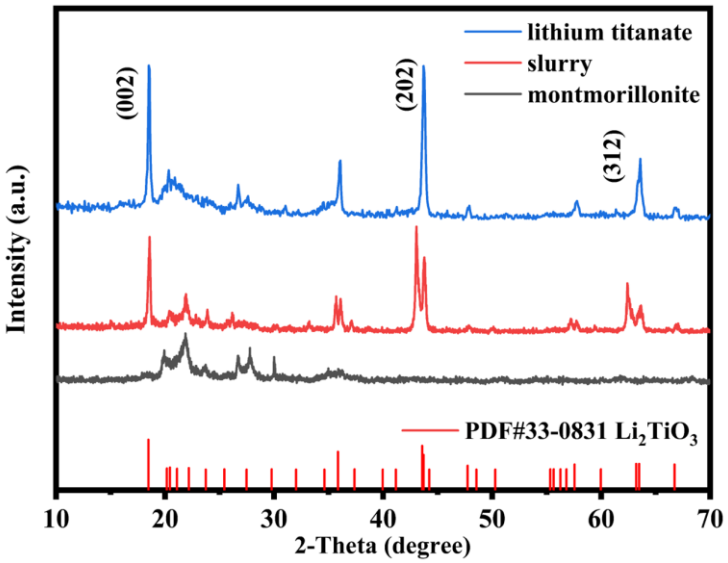

Figure 2. XRD of 3D printing slurry and its raw materials.

3.1.3. Stability and repeatability

In addition, the stability of the adsorbent was evaluated. As shown in Figure 3a, the thermal treatment temperature had a pronounced effect on the thermal stability of the adsorbent. The sample treated at 300 °C exhibited rapid mass loss and was almost completely depleted within approximately 60 h. The 400 °C sample remained relatively stable at the initial stage but showed evident and rapid mass loss after about 110 h. The 500 °C sample maintained a nearly constant mass until approximately 130 h, followed by a marked decrease. In contrast, the sample treated at 600 °C retained almost unchanged mass throughout the entire test, indicating excellent thermal stability and structural integrity. These results suggest that increasing the heat-treatment temperature is beneficial for enhancing the long-term stability of the adsorbent.

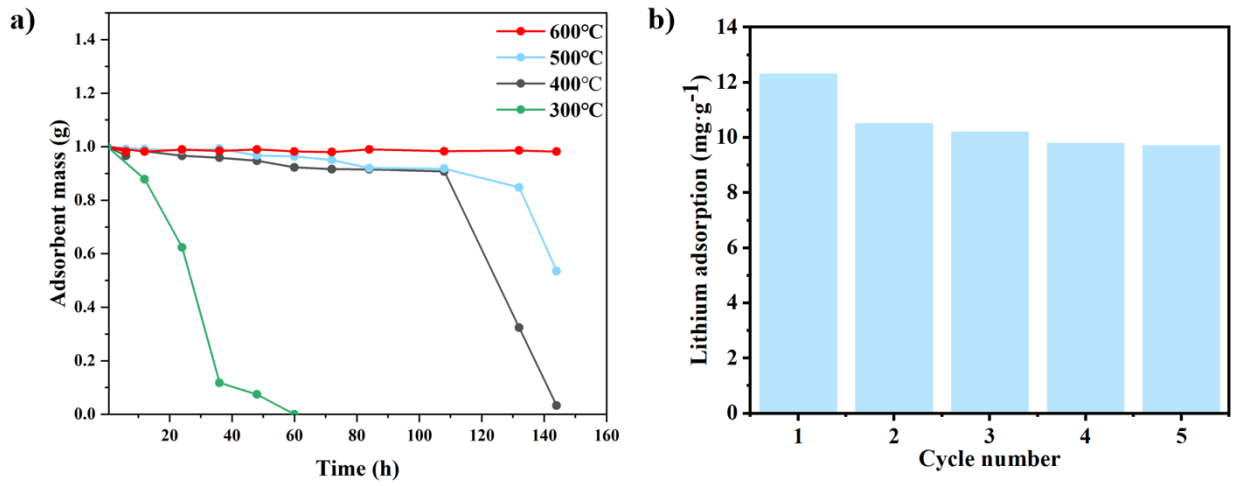

Figure 3. Reusability of the adsorbent: **(a)** The quality change curve of the adsorbent over time; **(b)** Cycle performance test.

Similarly, the cycling performance of the adsorbent was investigated, and the results are shown in Figure 3b. The lithium adsorption capacity in the first cycle was approximately 12.2 mg/g, and then slightly decreased in the subsequent cycles, remaining in the range of approximately 9.6–10.4 mg/g during the 2nd to 5th cycles. Although a certain degree of capacity decay was observed, the adsorbent still retained a relatively high lithium uptake after repeated use, demonstrating good reusability and cycling stability. Furthermore, as shown in Figure S2, we also supplemented the adsorption stability of the fixed bed. It can be observed that after 6 cycles, the fixed bed was able to maintain a relatively good adsorption level. Overall, the material exhibits promising potential for practical applications in terms of both thermal stability and cyclic performance.

3.2. Machine learning data analysis

3.2.1. Coding process of 3D printing monolithic adsorbent

In this work, a survey was conducted on the literature related to the adsorption method for lithium recovery from salt lakes and the methods of adsorbent formation over the past decade. A literature dataset was constructed by conducting keyword searches in the Web of Science database. As shown in Figure 4,

these literatures cover four different research topics: lithium recovery, the combination of lithium recovery and adsorption, and the combination of lithium recovery and brine. According to this data, the number of lithium recovery research papers has shown a significant growth trend over time, especially after 2018, with a substantial increase in the number of research papers. This phenomenon indicates that during this period, the research on adsorption method for lithium recovery from salt lakes began to receive widespread attention. In 2020, the number of research papers on adsorption-based lithium recovery reached 100, and then from 2021 to 2024, the number of research papers on the combination of lithium recovery and adsorption as well as the combination of lithium recovery and brine gradually increased, indicating that the research in this field has gradually entered a stable development stage.

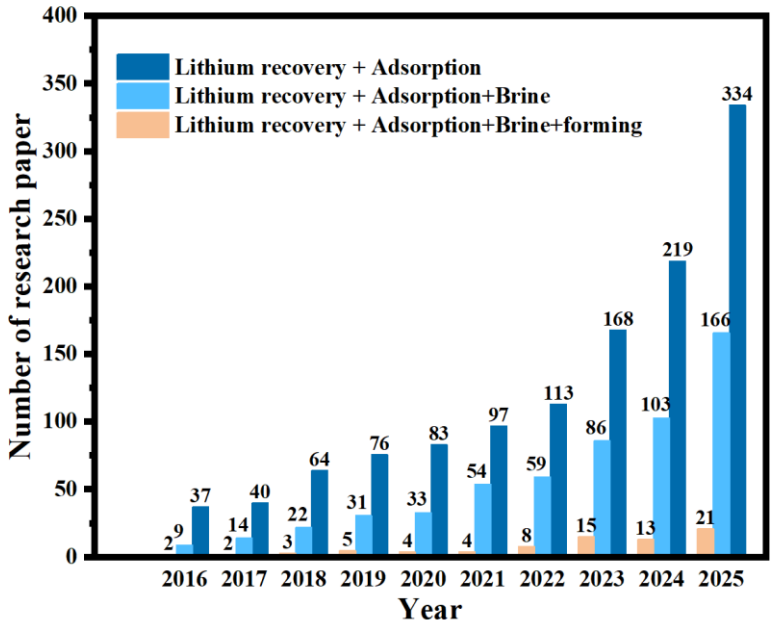

Figure 4. Summary of literatures in recent ten years.

In this study, a combination of coding methods was used to integrate the literature investigation data and experimental data into a one-dimensional vector for subsequent algorithm processing. As shown in Figure S3, the code mainly consists of the following parts: (1) The first part uses the method of unique thermal coding to classify and label the adsorbent forming process; (2) The second part represents the difference between different materials through Langmuir adsorption constant, and extracts the process parameters and 3D printing parameters of fixed bed parameters; (3) The outlet concentration of fixed bed was classified by numerical feature standardization method: $0 \leq C_t/C_0 < 0.25$ was category 1, $0.25 < C_t/C_0 \leq 0.5$ was category 2, $0.5 < C_t/C_0 \leq 0.75$ was category 3, and $0.75 < C_t/C_0 \leq 1$ was category 4.

In this work, box-whisker diagram is used for data preprocessing. The box diagram can clearly reflect the central trend, dispersion degree and outliers of the data. As shown in Figure 5a, the box whisker plot of the Langmuir constant shows a range roughly between 0.1 and 0.3, with relatively concentrated data but some significant outliers. These outliers may be due to differences in lithium recovery materials. In this work, these outliers are removed to ensure that the model does not overfit when using the data set. Figure 5b–d shows the box whisker diagrams encoded by different forming methods. Since this work adopts the unique thermal coding method to represent the three forming methods of powder, direct ink writing (DIW) and digital light processing (DLP), the box whisker diagrams are mainly distributed in the interval of 0 and 1.

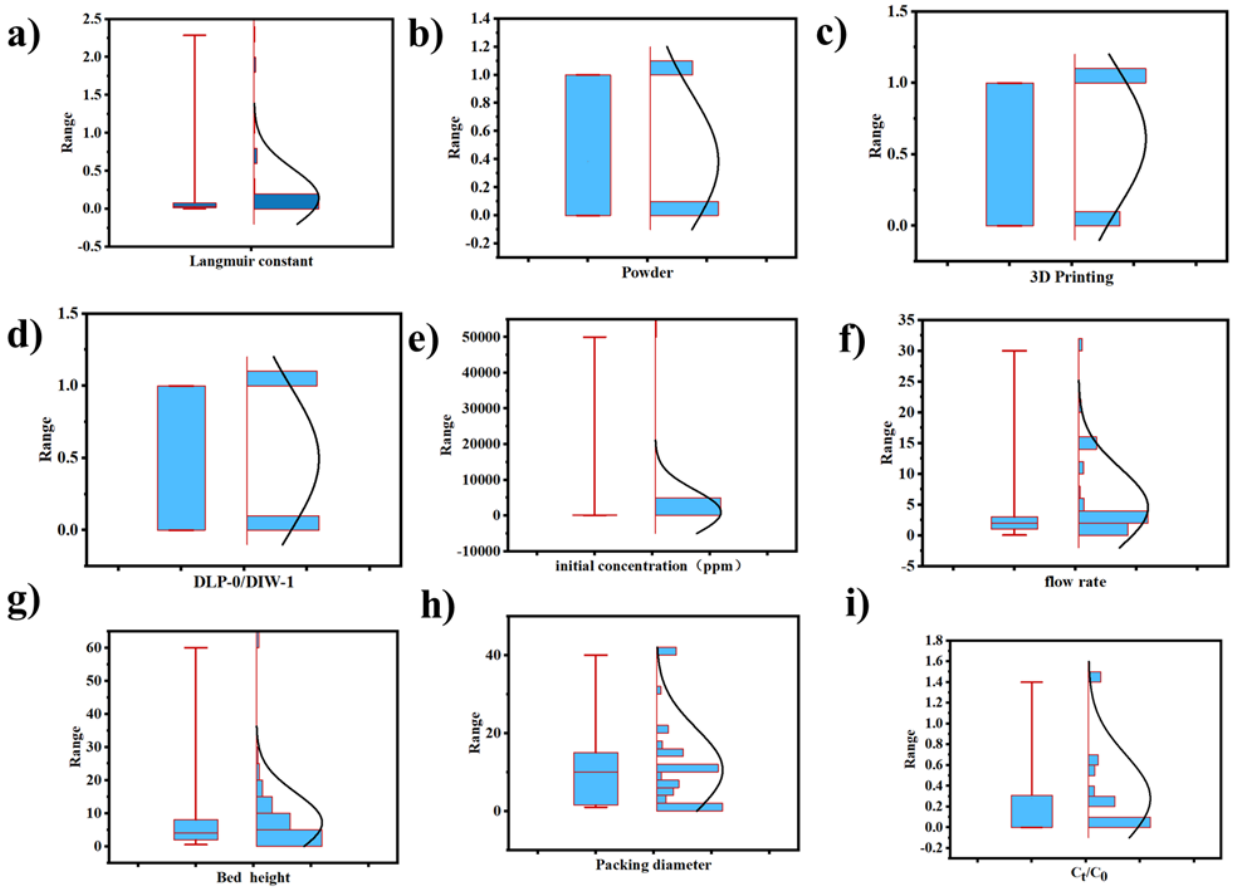

Figure 5. Data distribution in the constructed data set: **(a)** Box-whisker diagram of Langmuir adsorption constants; **(b)** Box whisker diagram of powder; **(c)** Box diagram of granulation; **(d)** 3D-printed box whisker diagram; **(e)** Box-whisker diagram of initial concentration; **(f)** Box whisker diagram of packing diameter; **(g)** Box diagram of inlet flow rate; **(h)** Box-whisker diagram of the storey height; **(i)** Box whisker diagram of needle diameter constant; **(j)** Box diagram of packing density; **(k)** Box-whisker diagram of adsorption time; **(l)** Box-whisker diagram of outlet concentration.

Figure 5e shows the box diagram of the initial concentration. It can be found that most of the concentrations are concentrated within 500 ppm, and occasionally some studies are higher than the data. Similarly, in order to prevent the influence of outliers on the machine learning model, these outliers are removed in this work. Figure 4f shows the distribution of inlet velocity. It can be found that the internal velocity selected by most literature ranges from 1–5 mL/min, indicating that the velocity may be optimal in this range. Figure 5g represents bed layers of different height, which indicates that the selection of bed layers during the fixed bed adsorption process may favor a higher setting. Figure 5h shows the diameter of the packing material. It can be found that most of the diameter of the packing material is within the range of 40 mm. Figure 5i represent the box whisker plots of adsorption time and C_t/C_0. The data of C_t/C_0 is also concentrated, indicating that the adsorption rate of most adsorbents is in a faster range.

3.2.2. Analysis of BP and RBF

After data set coding and outlier elimination, BP neural network and RBF neural network are used to predict the performance of fixed bed. The model constructed by inputting Langmuir adsorption constants and fixed bed process parameters can effectively predict the adsorption concentration at the outlet. As shown in Figure 6a and Figure 6c, compared with BP neural network, RBF neural network has a higher prediction effect on the data of the test set. Similarly, as shown in Figure 6b,d, the calculation accuracy of RBF neural network in training set is also higher than that of BP neural network. This is due to the fact that RBF neural networks employ radial basis functions as activation functions, allowing them to capture complex nonlinear relationships more efficiently. As a result, RBF networks can more flexibly fit the complex mapping relationship between input and output. In addition, the RBF network presents a Gaussian distribution feature by comparing the position of the input parameters with the center vector, and thus has a good sensitivity to the local features of the input space. In contrast, the global nature of BP networks may lead to underfitting in some regions. Furthermore, the Root Mean Square Error (RMSE) and Mean Absolute Error (MAE) values of different algorithms presented in Table S1 indicate that the prediction accuracy of RBF is even lower, which fully supports the aforementioned argument.

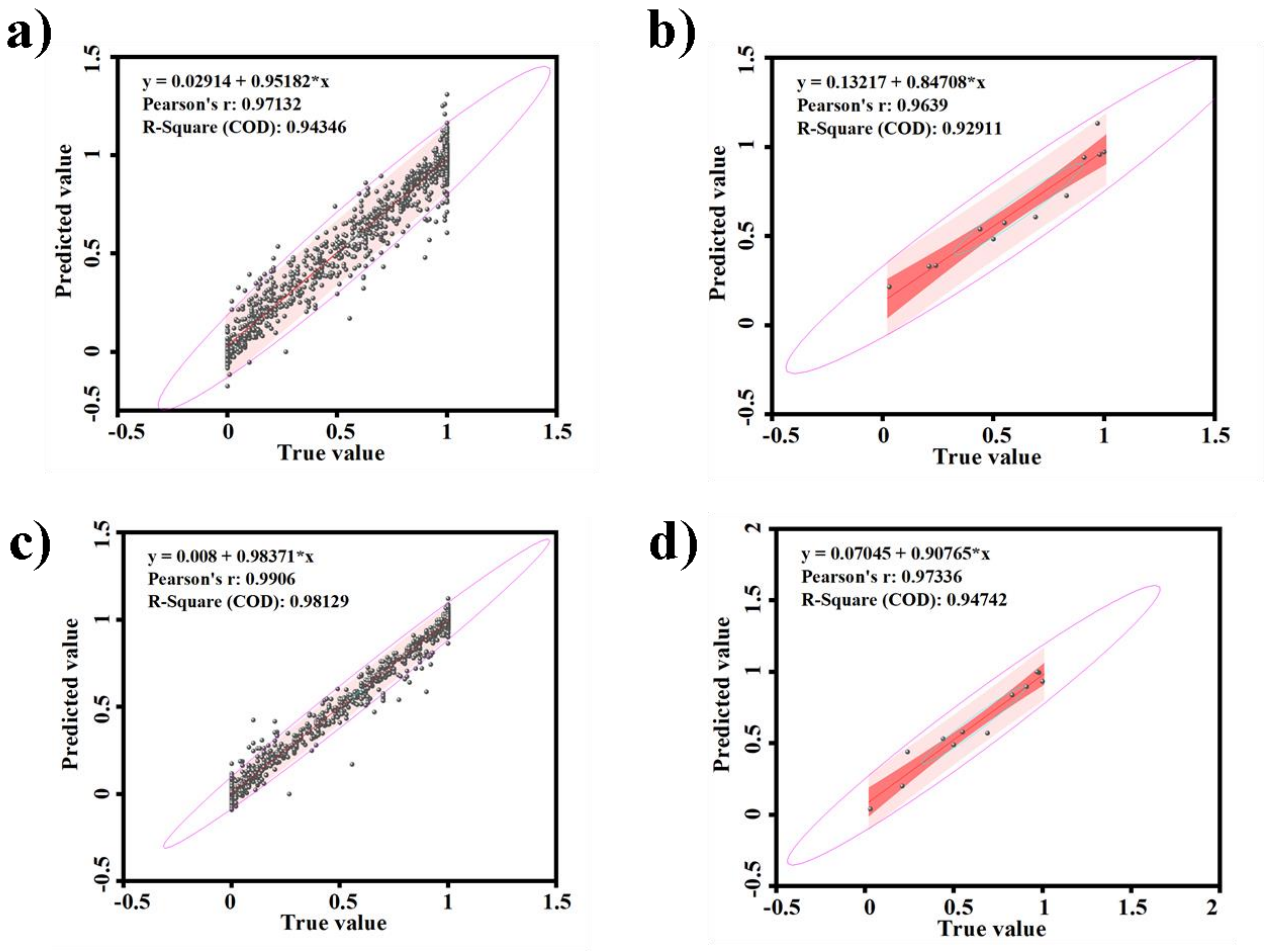

Figure 6. The calculation accuracy of the model: **(a)** Linear regression of R^2 of BP training set; **(b)** Linear regression of R^2 of BP test set; **(c)** Linear regression of R^2 of RBF training set; **(d)** Linear regression of R^2 of RBF test set.

3.2.3. Analysis of PNN and GRNN

Although BP and RBF neural networks can achieve accurate prediction of data, these two networks are composed of multiple levels and nodes, so a large number of data sets are usually required to improve the computational accuracy of the model. As a result, this kind of network has poor classification effect on small sample data. Therefore, in this work, probabilistic neural network and generalized regression neural network models based on statistical learning are used to classify the parameters of fixed bed.

In this work, 30 samples were randomly selected to predict the model. The C_t/C_0 values of the fixed bed were divided into four parts: $0 \leq C_t/C_0 < 0.25$ was class 1, $0.25 < C_t/C_0 \leq 0.5$ was class 2, $0.5 < C_t/C_0 \leq 0.75$ was class 3, and $0.75 < C_t/C_0 \leq 1$ was class 4. As shown in Figure S4a, by comparing the decision classification boundary analysis of PNN and GRNN, it can be found that the decision boundary of GRNN is smoother and can better adapt to changes in local data, which makes it perform well on complex data sets. However, the decision boundary of PNN is dependent on probability density estimation, resulting in good performance in data-intensive regions, but there may be misclassification at the boundary. This phenomenon shows that GRNN performs better than PNN in classification near the boundary, but PNN has higher classification accuracy in data-dense regions.

In addition, by analyzing the confusion matrix data of PNN and GRNN, the performance of the two neural networks under different conditions is evaluated. As shown in Table 1, the accuracy rate of the GRNN model under different conditions ranges from 0.93 to 0.98, indicating that the model performs relatively well in identifying positive samples. In particular, in the first set of data, the accuracy rate reached 0.98, indicating that almost all of the samples predicted to be positive were correct. On the whole, the number of false positive examples of GRNN is relatively small, indicating its high accuracy in classification.

Table 1. Confusion matrix data for PNN and GRNN.

	GRNN					PNN			
True positive	167	226	354	226	True positive	167	226	342	225
False positive	3	15	12	9	False positive	4	15	11	11
True negative	6	15	17	1	True negative	6	26	29	2
False negative	836	756	629	776	False negative	835	745	630	774
Accuracy	0.98	0.93	0.96	0.96	Accuracy	0.98	0.94	0.97	0.95

3.2.4. Classification process of CompNN

In order to evaluate the quality of the data set after the coding of the data set, this paper uses the competitive neural network (CompNN) to classify the data set. As shown in Figure S4b, after self-classification. All samples are divided into ten clustering centers, where the second cluster center contains 10% of the samples, the fifth cluster center contains 70% of the samples, and the ninth cluster center contains 15% of the samples. By combining the types of the data, it can be found that 2 types of samples belong to the bed adsorption zone, 5 types belong to the bed mass transfer zone, and 9 types belong to the bed depletion zone. In addition, it can be found that the fixed bed data presents a data distribution similar to the normal distribution (Figure S5).

3.2.5. The analysis of importance

After the prediction and classification of the data was completed, the random-forest approach was used to assess the importance of the fixed bed data extracted from the literature. The input parameters of the model include the following parts: (1) Langmuir constant, which is used to evaluate the interaction between different adsorbents and adsorbents; (2) Forming methods, including granulation, powder and 3D printing, used to characterize the forming methods in the process of fixed bed packings; (3) Initial concentration, used to represent the concentration at the entrance of the fixed bed; (4) Packing diameter, representing the packing diameter of the monolithic adsorbent; (5) Inlet flow rate, representing the speed at the entrance of the fixed bed; (6) Height, used to indicate the height of the bed; (7) The diameter of the print head is the diameter of the extrusion of the printer; (8) Filling density, representing the proportion of filling and channel in the fixed bed; (9) Time, representing the sampling time at the exit of the fixed bed.

3.2.6. Accuracy of RF algorithm

After completing the construction of the RF model, this study first verified the calculation accuracy and rationality of the RF model through the linear regression graph. As shown in Figure S4, the predicted value shows an obvious linear relationship with the true value. In addition, the determination coefficient $R^2 = 0.92$ indicates that the RF model constructed in this work is reasonable and has good prediction effect.

3.2.7. Eigencoefficient matrix of RF algorithm

Compared with artificial neural networks, the main advantage of RF is that they can explore the correlation between input variables and judge the interaction between data accordingly (Figure S6). As shown in Figure 7a,b, the Langmuir adsorption constant is highly positively correlated with the needle diameter, indicating that the change of needle diameter will significantly affect the adsorption performance. At the same time, there is a complete negative correlation between 3D printing and powder, because the three forming methods of 3D printing, powder and granulation cannot exist at the same time in the coding process. The positive correlation between the initial concentration and 3D printing indicates that there is a certain dependence between the initial concentration and 3D printing. The reason may be that the 3D printing monolithic adsorbent can achieve faster mass transfer, making the 3D printing monolithic adsorbent very sensitive to the concentration of the adsorbent. In addition, the relationship between time and other characteristics is more complex, especially the negative correlation between time and 3D printing and initial concentration. The reason is that when 3D printing is selected as a forming strategy and a higher concentration is selected, the adsorption rate will be greatly increased, making the adsorbent reach adsorption equilibrium in a very short time. The relationship between these variables has a certain guiding significance for the optimization and design of subsequent process parameters.

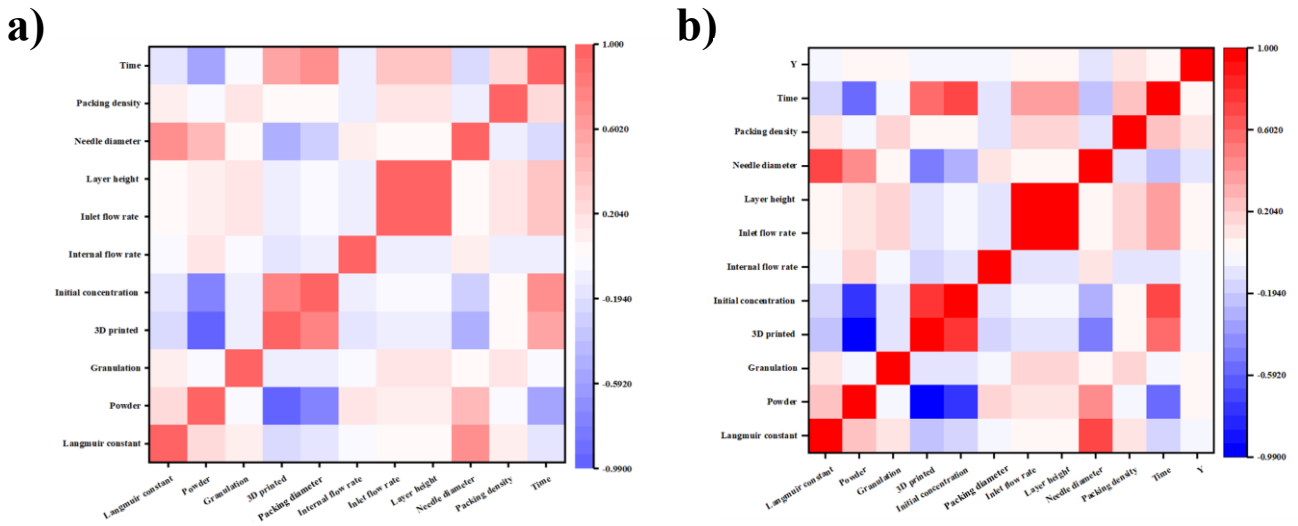

Figure 7. Feature representation and inter-variable correlation analysis of the dataset: **(a)** Feature matrix; **(b)** Pearson correlation coefficient matrix.

3.2.8. Feature analysis of RF algorithm

This work evaluated the importance of input features using the RF algorithm. As shown in Figure 8, it indicates the relative importance of different features evaluated by the RF algorithm for the model. This study classified the above 11 input parameters into five factors: material parameters, molding strategies, process parameters, printing parameters, and time factors. The importance ranking of these five factors is mainly as follows: time factors > printing parameters > process parameters > molding strategies > material parameters. Analyzing these factors leads to the following hypotheses: (1) For the fixed-bed adsorption process, the structure of the packing will affect the diffusion rate of solute molecules within the packing and the size of droplets within the packing, thereby significantly affecting the outlet concentration; (2) The Langmuir adsorption constant affects the rate at which solute molecules diffuse from the surface of the adsorbent to the interior of the adsorbent, thereby affecting the outlet concentration; (3) Flow rate and initial concentration affect the residence time and concentration of solute molecules on the adsorbent surface, thereby affecting the adsorption process; (4) The adsorption time is the key factor affecting the residence time of solute molecules on the adsorbent surface; (5) The molding strategy has the least influence because each molding strategy has its advantages and disadvantages, such as the filling density of granulation being high but the mass transfer rate being slow, and powder molding having a fast mass transfer but the fluid being difficult to penetrate the bed; in addition, by analyzing the single-factor process, it can be found that in the single-factor process, except for the time factor, the bed height and flow rate have a greater impact compared to the material factors. The main reason is that in the fixed-bed process, the liquid film mass transfer efficiency affects the key of the dynamic adsorption process.

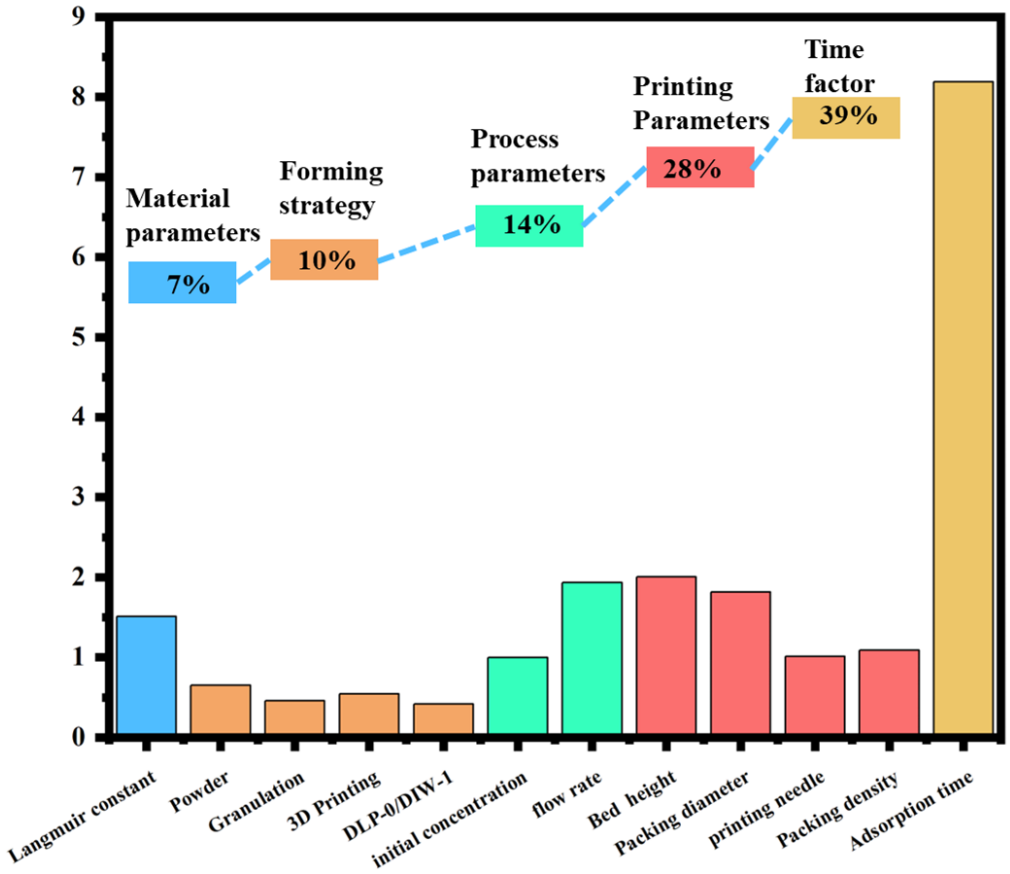

Figure 8. Importance of each feature to the output value.

3.2.9. Selection of the optimal structure

Although the input parameters of the adsorption process have been evaluated in the above studies, the optimal parameters of the adsorption process have not been selected. Therefore, GA and response surface method were used in this study to optimize and select the optimal parameters of the adsorption process.

In this study, RBF artificial neural network is used as fitness function, and GA is used to optimize the data iteratively, so as to design and prepare the integrated adsorbent structure. The detailed parameters of GAs are described in the RBF-GA architecture in the first part of this paper. As shown in Figure S7, the optimal structural parameters selected by RBF-GA method are as follows: needle diameter 0.13 mm, adsorbent diameter 12.5 mm, packing density 0.3, adsorption time 190 min. The response surface method shows that the above optimal conditions fall on the optimal response surface of the response surface. Although GA can screen and optimize better structural parameters than response surface method, GA is difficult to analyze the influence process of each input factor on the result. Therefore, in this study, the response surface method will also be used to explore the impact of 3D printing structural parameters on adsorption properties.

3.3. Experimental verification using response surface method

3.3.1. Variance analysis of response surface method

In this work, the experimental design principle of the response surface method adopted is based on the central composite design (CCD). The basic principle of CCD is to construct an effective experimental

design by combining the full factor design and the central point design, so as to facilitate the modeling and optimization of the response surface. In this work, ANOVA is used to verify the accuracy of the model.

In this study ANOVA in response surface method (RSM) was used to evaluate the impact of different factors on response variables and their significance to analyze the overall performance of the model. As shown in Table S1, the overall significance p-value of the model is less than 0.0001, indicating that there is a statistically significant relationship between at least one independent variable and the response variable. It can be found that the needle diameter has a significant influence, and its p-value is 0.0001, indicating that the needle diameter plays an important role in the change of response variables in this experiment. Because the size of the diameter directly affects the flow path in the fixed bed, and thus affects the adsorption process, this conclusion is similar to the conclusion obtained in RF. However, compared with the needle diameter, the p-value of packing diameter, filling density and time was greater than 0.05, indicating that the changes of these three factors had no significant effect on the experimental results within the measurement range. The reason may be that these parameters did not significantly change the outlet concentration, making it difficult for the response surface method to fully capture the influence of these parameters on the adsorption process.

In addition, the accuracy of the response surface method is verified by the regression graph between the predicted value and the actual value and the normal probability graph of the residual. As shown in Figure S6a, most points are concentrated near the slash line, indicating that the predicted value of the model is close to the true value. In addition, as shown in Figure S8, the residual distribution is close to a normal distribution. Regression analysis and residual analysis show that the response surface method has good accuracy.

3.3.2. Analysis of extrusion forming process

The response surface method is widely used in various fields due to its excellent fitting effect. This work mainly studies the influence of forming parameters and process parameters on the adsorption performance of the fixed bed by using the response surface method. As shown in Figure 9a, the surface of this graph shows an upward trend as the Langmuir constant and initial concentration increase, indicating that the increase in initial concentration provides more Li^+ for adsorption, and the increase in the Langmuir constant also facilitates the adsorption process, and the two work together to promote the increase in adsorption amount. As shown in Figure 9b, as the Langmuir constant increases, the adsorption amount rises, while the adsorption amount decreases when the flow rate increases. This is because the flow rate is too fast, which will cause insufficient contact time between lithium ions and the adsorbent, thereby reducing the adsorption amount.

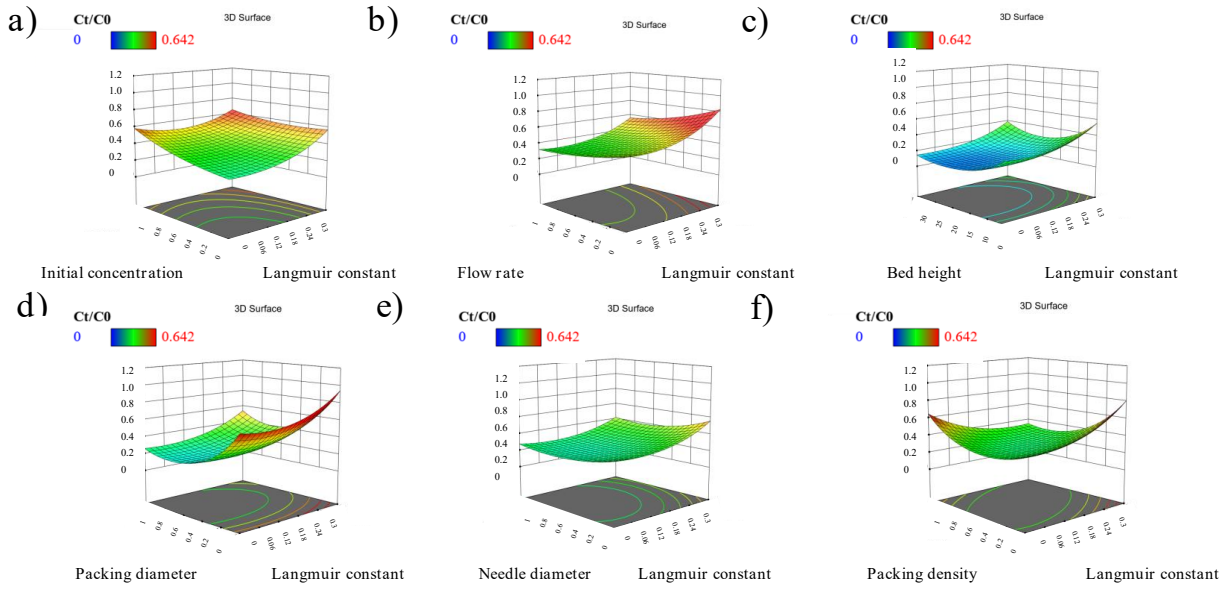

Figure 9. Response surface diagram for granulation molding: **(a)** Initial concentration–Langmuir constant; **(b)** Flow rate–Langmuir constant; **(c)** Bed height–Langmuir constant; **(d)** Packing diameter–Langmuir constant; **(e)** Needle diameter–Langmuir constant; **(f)** Packing density–Langmuir constant.

However, the increase in the Langmuir constant can to some extent compensate for the negative impact of the flow rate. As shown in Figure 9c, the adsorption amount increases when the Langmuir constant increases, and it decreases when the bed height increases. This indicates that an excessively high bed height may lead to a decrease in mass transfer efficiency, thereby affecting the adsorption amount. As shown in Figure 9d, the adsorption amount increases when the Langmuir constant and the particle diameter of the packing increase. The larger particle diameter may provide more adsorption sites, and combined with the effect of the Langmuir constant, it jointly increases the adsorption amount. As shown in Figure 9e, the adsorption amount increases when the Langmuir constant increases, and it first rises and then decreases when the print needle diameter increases. This indicates that there is an optimal value for the print needle diameter, and the adsorption effect is best near this value, and the adsorption amount decreases when deviating from this value. As shown in Figure 9f, the adsorption amount increases when the Langmuir constant increases, and it decreases when the packing density increases. This may be because the excessive packing density will lead to a deterioration of the pore structure, affecting the diffusion and adsorption of Li^+.

Furthermore, this study also compared the correlations among the process parameters. In Figure 10a, the relationship between flow rate, initial concentration and adsorption capacity shows that as the initial concentration increases, the adsorption capacity rises, while as the flow rate increases, the adsorption capacity decreases, indicating that the initial concentration provides more lithium sources, while a too fast flow rate reduces the contact time. In Figure 10b, in the interaction between bed height and initial concentration, the initial concentration increases the adsorption capacity, while the bed height increases the adsorption capacity decreases, reflecting that an excessively high bed height reduces the mass transfer efficiency. In Figure 10c, the combined effect of packing diameter and initial concentration

shows that both increasing leads to an increase in adsorption capacity, as a larger packing diameter provides more adsorption sites. In Figure 10d, the influence of print needle diameter and initial concentration is that the initial concentration increases the adsorption capacity, while the print needle diameter has an optimal value, and deviation leads to a decrease in adsorption capacity. In Figure 10e, the relationship between packing density and initial concentration is that as the initial concentration increases, the adsorption capacity rises, while as the packing density increases, the adsorption capacity decreases, due to the high density causing a deterioration of the pore structure. As shown in Figure 10f, initial concentration exerts a more pronounced effect on the response than adsorption time, while the relatively smooth surface suggests a limited interaction between these two variables. In contrast, Figure 10g–i exhibits more evident curvature in the response surfaces, together with elliptical contour lines, indicating significant quadratic effects and non-negligible interactions between bed height and the corresponding molding parameters. Among them, the coupling effects between bed height and filler diameter/filling density appear more prominent, whereas the interaction with needle diameter is relatively weaker. Overall, these results demonstrate that both bed-structure parameters and feed conditions play important roles in regulating the granulation molding process.

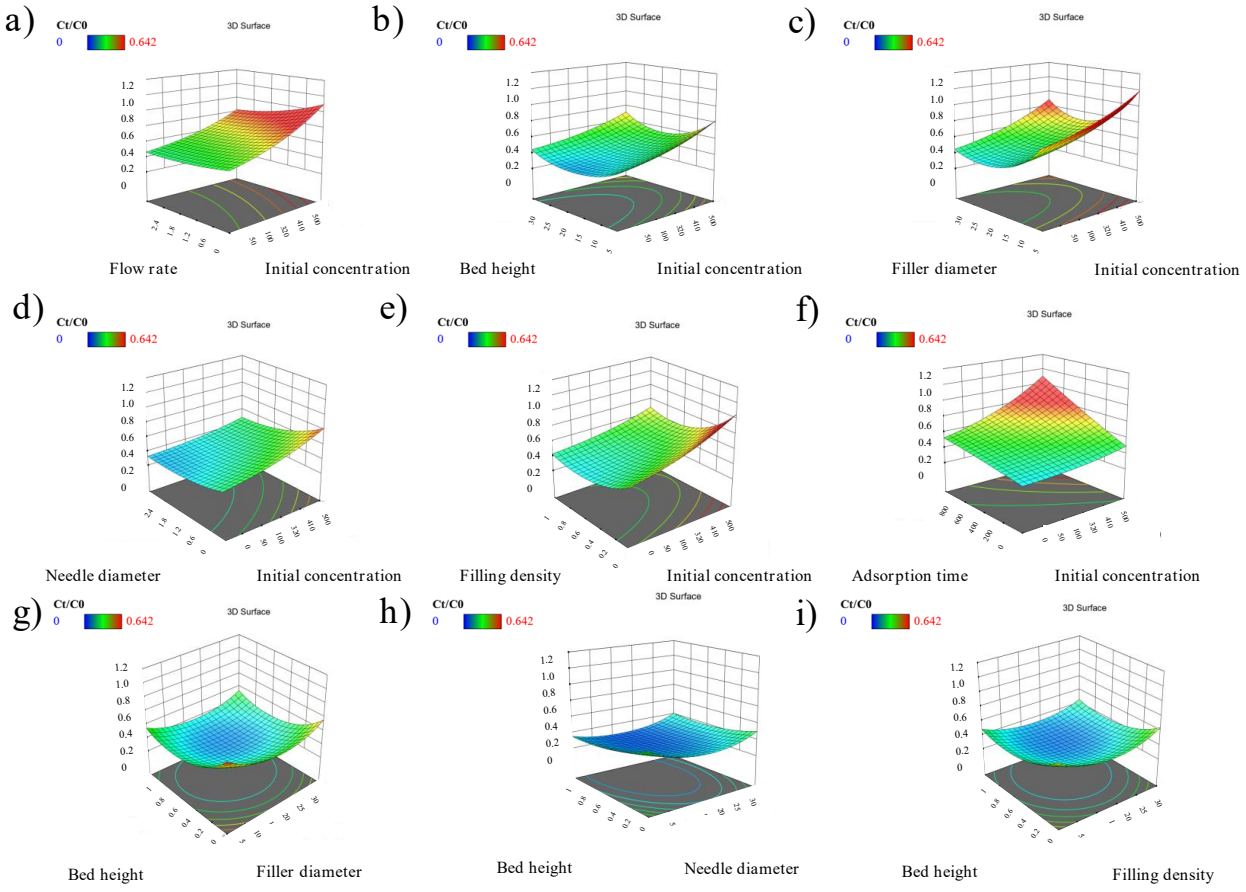

Figure 10. Response surface diagram for granulation molding: **(a)** Flow rate–Initial concentration; **(b)** Bed height–Initial concentration; **(c)** Filler diameter–Initial concentration; **(d)** Needle diameter–Initial concentration; **(e)** Filling density–Initial concentration; **(f)** Adsorption time–Initial concentration;**(g)** Bed height–Filler diameter; **(h)** Bed height–Needle diameter; **(i)** Bed height–Filling density.

3.3.3. Analysis of 3D printing forming process

The correlations between the packing parameters within the monolithic adsorbent and the performance of the fixed bed were also investigated in this work. As shown in the Figure 11a, under the interaction of the initial concentration and the Langmuir constant, the adsorption amount increases as both increase, indicating that the initial concentration provides more lithium sources, and an increase in the Langmuir constant is beneficial for the adsorption process; In Figure 11b, in the combination of flow rate and the Langmuir constant, an increase in the Langmuir constant leads to an increase in the adsorption amount, while an increase in the flow rate leads to a decrease in the adsorption amount, as the flow rate is too fast, reducing the contact time.

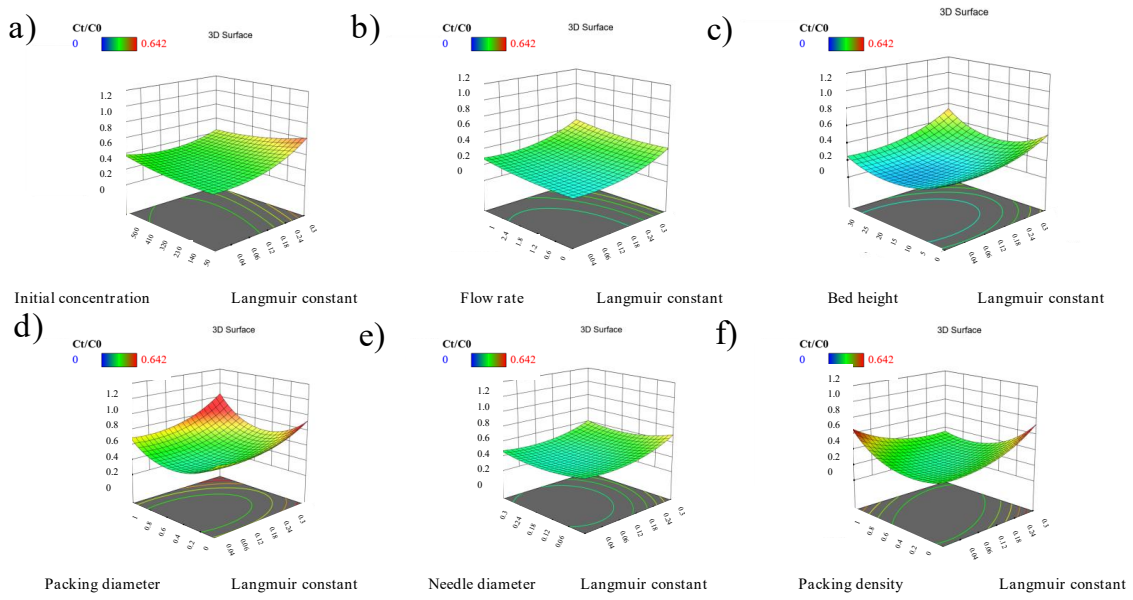

Figure 11. 3D-printed response surface diagram: **(a)** Initial concentration–Langmuir constant; **(b)** Flow rate–Langmuir constant; **(c)** Bed height–Langmuir constant; **(d)** Packing diameter–Langmuir constant; **(e)** Needle diameter–Langmuir constant; **(f)** Packing density–Langmuir constant.

In addition, as shown in Figure 11c, the interaction between bed height and the Langmuir constant causes an increase in the Langmuir constant and an increase in the adsorption amount, while an increase in bed height leads to a decrease in the adsorption amount, reflecting that an excessively high bed height reduces the mass transfer efficiency; in Figure 11d, the combined effect of the packing diameter and the Langmuir constant causes both to increase, resulting in an increase in the adsorption amount; larger packing diameters provide more adsorption sites; in Figure 11e, the influence of the print needle diameter on the Langmuir constant is such that an increase in the Langmuir constant leads to an increase in the adsorption amount, and there is an optimal value for the print needle diameter; deviation from this value leads to a decrease in the adsorption amount; in Figure 11f, the relationship between packing density and the Langmuir constant is that an increase in the Langmuir constant leads to an increase in the adsorption amount, while an increase in packing density leads to a decrease in the adsorption amount, due to excessive density resulting in a deterioration of the pore structure.

In addition to the influence of material parameters on the performance of the 3D printing integral adsorbent fixed bed, this work also investigated the effects of filler parameters and process parameters

on the fixed bed process. In Figure 12a, under the interaction of flow rate and initial concentration, the adsorption amount increases with the increase of initial concentration, and decreases with the increase of flow rate, reflecting the influence of initial concentration as a source of lithium and the reduction of contact time due to the excessive flow rate; in Figure 12b, in the combination of bed height and initial concentration, the adsorption amount increases with the increase of initial concentration and decreases with the increase of bed height, indicating that the excessively high bed height reduces the mass transfer efficiency; in Figure 12c, the filling diameter and initial concentration interactively affect each other. Both increasing the filling diameter and the initial concentration lead to an increase in the adsorption amount, as larger filling diameters provide more adsorption sites; in Figure 12d, the influence of the printing needle diameter and initial concentration is that the adsorption amount increases with the increase of initial concentration, and there is an optimal value for the printing needle diameter; deviations from this optimal value result in a decrease in the adsorption amount; in Figure 12e, the relationship between the filling density and initial concentration is that the adsorption amount increases with the increase of initial concentration and decreases with the increase of filling density, due to the excessive density causing a deterioration of the pore structure.

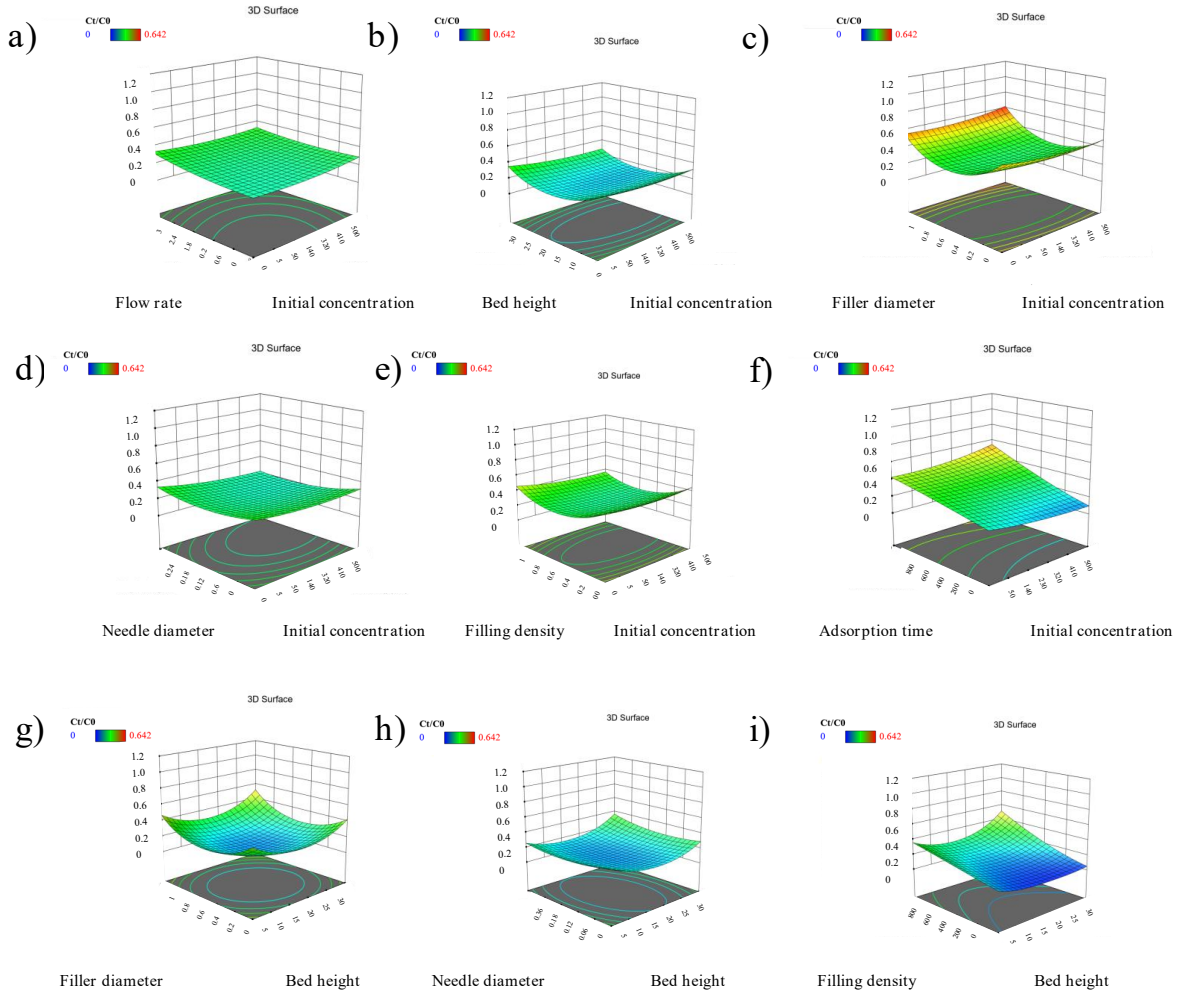

Figure 12. 3D-printed response surface diagram: **(a)** Flow rate–Initial concentration; **(b)** Bed height–Initial concentration; **(c)** Filler diameter–Initial concentration; **(d)** Needle diameter–Initial concentration; **(e)** Filling density–Initial concentration; **(f)** Adsorption time–Initial concentration; **(g)** Filler diameter–Bed height; **(h)** Needle diameter–Bed height; **(i)** Filling density–Bed height.

Furthermore, in Figure 12f, the interaction of adsorption time and initial concentration shows that the adsorption amount increases within a certain range of initial concentration and adsorption time, and the adsorption time is too long or reaches saturation; in Figure 12g, under the combination of filling diameter and bed height, the adsorption amount shows a trend of increasing first and then decreasing, indicating that there is a synergistic optimal range between the two; in Figure 12h, the interaction of the printing needle diameter and bed height causes a significant change in the adsorption amount, reflecting the influence of the matching of the printing needle diameter and bed height on the adsorption effect; in Figure 11i, the relationship between the adsorption time and bed height shows that the adsorption amount changes with the variation of the two, reflecting the comprehensive regulation of the combination of adsorption time and bed height on the adsorption process.

3.4. Limitations of the present study

The main limitation of this work lies in the fact that the current dataset is dominated by titanium-based lithium ion-sieves, with relatively limited diversity in adsorbent types and brine systems. As a result, the generalization capability of the proposed model for other ion-sieves, such as manganese-based and manganese–titanium composite materials, remains limited. In addition, although ensemble models such as RF provide high predictive accuracy, they are essentially black-box models, and the quantitative relationship between model parameters and liquid-film mass transfer mechanisms has not yet been fully clarified. Further mechanistic interpretation with the aid of CFD is still required. Moreover, the optimization framework developed in this study is mainly applicable to fixed-bed adsorption systems and cannot be directly transferred to other lithium extraction processes, such as membrane separation or electrochemical lithium recovery. In future work, we will expand the dataset to include multiple adsorbents and diverse brine systems, and integrate explainable artificial intelligence (XAI) approaches to improve model transparency and generalizability.

4. Conclusions

This study addresses the lithium resource demand gap resulting from the rapid development of the lithium battery industry, focusing on the adsorption bed process for extracting lithium from salt lake brine. It is the first time that machine learning has been applied to analyze the shaping strategy of the adsorbent and optimize the filling structure. Using lithium titanate as the adsorbent and montmorillonite as the binder, the adsorbent materials were prepared through processes such as granulation and 3D printing. The spherical structure and crystal stability of the materials were verified using SEM and XRD techniques. Based on the literature data, a dataset was constructed and preprocessed through encoding, outlier removal, *etc.* Then, neural networks such as BP, RBF, PNN, GRNN, and RF algorithms were used to systematically analyze the influence of shaping methods, process parameters, and material characteristics on the performance of the adsorption bed. It was found that the prediction accuracy of the RBF neural network was superior to that of the BP network, and the GRNN performed particularly well in small sample classification. The RF algorithm confirmed that the importance ranking of influencing factors was time factor > printing parameters > process parameters > shaping strategy > material parameters, and the influence of liquid film mass transfer efficiency on the performance of the adsorption bed was much greater than that of the material itself. The optimal structural parameters (filling diameter

12.5 mm, density 0.3, printing needle diameter 0.13 mm, adsorption time 190 min) were selected through the RBF-GA model and response surface method. The model was verified to be accurate and reliable, and it clarified that the optimization of the adsorption bed should prioritize the design of the filling structure to improve the liquid film mass transfer efficiency. It also accumulated important experience for the application of machine learning in material shaping.

Supplementary data

The authors confirm that the supplementary data are available within this article. This supporting material provides supplementary data and detailed methods based on which the main findings of the text are derived. It covers the structure and CFD simulation of the integral adsorbent (Figures S1 and S2), 3D printing encoding schemes (Figure S3), as well as the performance evaluation of various machine learning models, including the classification boundaries of PNN and GRNN (Figure S4), the classification results of CNN (Figure S5), RF regression (Figure S6), the fitness evolution of GA and RSM optimization (Figures S7). The accuracy of response surface method (Figures S8). Additionally, Table S1 summarizes ANOVA results of the response surface quadratic model, and Table S2 lists the comparative prediction errors of RBF neural networks under different transfer functions and training algorithms; These supplementary results collectively support the model accuracy, optimization strategies, and operational reliability of the proposed machine learning-driven ion sieve molding strategy in lithium extraction from salt lakes.

Data availability statement

The data or datasets generated or analyzed in this study are available in ScienceDB at https://www.scidb.cn/anonymous/NnpRdmVx.

Declaration of generative AI and AI-assisted technologies

During the preparation of this manuscript, the authors used generative AI tools only to improve language and readability. Specifically, the authors used ChatGPT, Deepseek and Doubao for language polishing only for drafting, development in limited sections. The authors take full responsibility for the content of the manuscript.

Acknowledgments

This work was financially supported by the National Natural Science Foundation of China (Grant No. 22462031) (funding acquisition: Feng Gao). Huyang Talent Award—Research Startup Grant for Introduced Talents (Doctoral Level) Project (Grant No. TDZKBS202647) (funding acquisition: Jiangtao Yu). 2024 Annual Shaoyang City Science and Technology Plan Project (Grant 508 No. 2024PT6114) (funding acquisition: Weihua Hong). Presidential Research Fund of Tarim University (No. TDZKBS202547); Talent Project of Xinjiang Uyghur Autonomous Region (Tianchi Talents) (No. BT-2025-TCYC-0055) (funding acquisition: Zegang Fu).

Authors' contribution

Jiangtao Yu: investigation, methodology, writing—original draft, writing–review and editing; Zegang Fu: conceptualization, methodology, writing—review and editing; Pakiza Ajibek: conceptualization, methodology; Meng Zhang: conceptualization, methodology; Weihua Hong: conceptualization, methodology, writing—review and editing; Feng Gao: conceptualization, methodology, writing—review and editing.

Conflicts of interest

The authors declare that they have no known competing financial interests or personal relationships that could have appeared to influence the work reported in this paper.

References

[1] Neumann I, Rasche B. *In situ* diffraction in electrochemistry–a practical introduction for experiments beyond batteries. *Curr. Opin. Electrochem.* 2023, 39:101288.

[2] Weng Y, Liu H, Pei A, Shi F, Wang H, *et al.* An ultrathin ionomer interphase for high efficiency lithium anode in carbonate based electrolyte. *Nat. Commun.* 2019, 10(1):5824.

[3] Wang Q, Lu T, Xiao Y, Wu J, Guan L, *et al.* Leap of li metal anodes from coin cells to pouch cells: challenges and progress. *Electrochem. Energy Rev.* 2023, 6(1):22.

[4] Shakoor N, Adeel M, Ahmad MA, Zain M, Waheed U, *et al.* Reimagining safe lithium applications in the living environment and its impacts on human, animal, and plant system. *Environ. Sci. Ecotechnol.* 2023, 15:100252.

[5] Mends EA, Chu P. Lithium extraction from unconventional aqueous resources—a review on recent technological development for seawater and geothermal brines. *J. Environ. Chem. Eng.* 2023, 11(5):110710.

[6] Wu L, Zhang C, Kim S, Hatton TA, Mo H, *et al.* Lithium recovery using electrochemical technologies: advances and challenges. *Water Res.* 2022, 221:118822.

[7] Zhang T, Zheng W, Wang Q, Wu Z, Wang Z. Designed strategies of nanofiltration technology for Mg2+/Li+ separation from salt-lake brine: a comprehensive review. *Desalination* 2023, 546:116205.

[8] Michl J, Sykes ECH. Molecular rotors and motors: recent advances and future challenges. *ACS Nano* 2009, 3(5):1042–1048.

[9] Pramanik BK, Long Duc N, Hai FI. Extraction of strategically important elements from brines: constraints and opportunities. *Water Res.* 2020, 168:115149.

[10] Swain B. Recovery and recycling of lithium: a review. *Sep. Purif. Technol.* 2017, 172:388–403.

[11] Liu Q, Yang P, Tu W, Sun H, Li S, *et al.* Lithium recovery from oil and gas produced water: opportunities, challenges, and future outlook. *J. Water Process Eng.* 2023, 55:104148.

[12] Kim N, Su X, Kim C. Electrochemical lithium recovery system through the simultaneous lithium enrichment via sustainable redox reaction. *Chem. Eng. J.* 2021, 420:127715.

[13] Chen M, Zeng T, Liu Y, Liu R. Extraction of lithium in salt lake brine through highly selective titanium ion sieves—a review. *Funct. Mater. Lett.* 2022, 15(07N08):2250030.

[14] Hsiang H, Chen W. Electrochemical properties and the adsorption of lithium ions in the brine of lithium-ion sieves prepared from spent lithium iron phosphate batteries. *Sustainability* 2022, 14(23):16235.
[15] Arby DS, Chung E, Jang Y, Lee J. $LiNi_xMn_2$-xO_4 for multicycle electrochemical selective recovery of lithium from lithium-ion battery leachate. *Sep. Purif. Technol.* 2023, 323:124453.
[16] Knapik E, Rotko G, Marszalek M. Recovery of lithium from oilfield brines-current achievements and future perspectives: a mini review. *Energies* 2023, 16(18):6628.
[17] Khatoon R, Raksasat R, Ho YC, Lim JW, Jumbri K, *et al.* Reviewing advanced treatment of hydrocarbon-contaminated oilfield-produced water with recovery of lithium. *Sustainability* 2023, 15(22):16016.
[18] Sorour MH, Hani HA, El Sayeda MMH, Al Bazedi GA. Towards lithium recovery from desalination brines via an integrated scheme. *Desalin. Water Treat.* 2017, 61:311–318.
[19] Zhao K, Li J, Yuan J, Yu X, Guo Y, *et al.* A novel Co-doped H2TiO3 spinning composite for efficient lithium recovery from alkaline lithium precipitation mother liquor. *Chem. Eng. J.* 2024, 482:148989.
[20] Wang P, Dai J, Ma Y, Chen L, Pan J. Fabrication and evaluation of aminoethyl benzo-12-crown-4 functionalized polymer brushes adsorbents formed by surface-initiated ATRP based on macroporous polyHIPEs and postsynthetic modification. *Chem. Eng. J.* 2020, 380:122495.
[21] Wang S, Chen X, Zhang Y, Zhang Y, Zheng S. Lithium adsorption from brine by iron-doped titanium lithium ion sieves. *Particuology* 2018, 41:40–47.
[22] Aburabie J, Mohammed S, Hashaikeh R. Chelating packed bed adsorption column for selective trace metal recovery from seawater and brine. *Sep. Purif. Technol.* 2025, 369:133112.
[23] Ding T, Wu Q, Nie Z, Zheng M, Wang Y, *et al.* Selective recovery of lithium resources in salt lakes by polyacrylonitrile/ion-imprinted polymer: synthesis, testing, and computation. *Polym. Test.* 2022, 113:107647.
[24] Gao Y, Wang S, Gao F, Guo C, Dong J, *et al.* Al and Cr ions co-doped spinel manganese lithium ion-sieve with enhanced Li plus adsorption performance and structural stability. *Microporous Mesoporous Mater.* 2023, 351:112492.
[25] Liu Z, Chen K, Ding J, Wang W, Lu J. The modification of MnO2.0.5H2O by Al/Mg doping to enhance lithium adsorption and reduce manganese dissolution with application to brines. *Hydrometallurgy* 2023, 219:106078.
[26] Recepoglu YK, Yuksel A. Cross-linked phosphorylated cellulose as a potential sorbent for lithium extraction from water: dynamic column studies and modeling. *ACS Omega* 2022,7(43): 38957–38968.
[27] Ren Y, Zhao D, Zhou F, Liu Y, Fu C, *et al.* MXene-bridged HMO/PSF adsorptive membrane for selective lithium recovery from shale gas wastewater with suppressed Mn leaching. *Desalination* 2025, 600:118515.
[28] Zhao M, Luan J, Zhao C, Zhang Y, Pan G, *et al.* Highly selective granulation adsorbents for lithium recovery from gas field brine: selectivity, kinetics and mechanism. *Desalination* 2024, 583:117699.
[29] Yu J, Zhu J, Luo G, Chen L, Li X, *et al.* 3D-printed titanium-based ionic sieve monolithic adsorbent for selective lithium recovery from salt lakes. *Desalination* 2023, 560:116651.
[30] Yoo H, Kim C, Song J, Hong H. Acid-free strategy for lithium(Li) extraction from saline groundwater using hydrogen manganese oxide-immobilized carboxymethylated cellulose nanofibril (HMO@CMCNF) membrane. *Chem. Eng. J.* 2025, 516:164131.

[31] Zhao M, Luan J, Zhao C, Zhang Y, Pan G, *et al.* Highly selective granulation adsorbents for lithium recovery from gas field brine: selectivity, kinetics and mechanism. *Desalination* 2024, 583:117699.
[32] Torres D, Perez K, Madrid FMG, Leiva WH, Galvez E, *et al.* Salar de atacama Lithium and potassium productive process. *Metals* 2024, 14(10):1095.
[33] Sujoto VSH, Prasetya A, Petrus HTBM, Astuti W, Jenie SNA, *et al.* Advancing Lithium extraction: a comprehensive review of titanium-based Lithium-Ion sieve utilization in geothermal brine. *J. Sustainable Metall.* 2024, 10(4):1959–1982.
[34] Lansford JL, Vlachos DG. Infrared spectroscopy data-and physics-driven machine learning for characterizing surface microstructure of complex materials. *Nat. Commun.* 2020, 11(1):1513.
[35] Liu Y, Yang Y, Chen W, Shen F, Xie L, *et al.* DeepRTAlign: toward accurate retention time alignment for large cohort mass spectrometry data analysis. *Nat. Commun.* 2023, 14(1):8188.
[36] Syu MJ, Tsai GJ, Tsao GT. Artificial neural network modeling of adsorptive separation. In *Chromatography*. Berlin: Springer Berlin Heidelberg, 1993, pp. 97–122.
[37] Raccuglia P, Elbert KC, Adler PDF, Falk C, Wenny MB, *et al.* Machine-learning-assisted materials discovery using failed experiments. *Nature* 2016, 533(7601):73–76.
[38] Chen X, Su J, Li Y. Application of a niching genetic algorithm to the optimization of a SiC crystal growth system. *J. Mater. Sci.: Mater. Electron.* 2017, 28(1):269–275.
[39] LoftiKatooli L, Shahsavand A. Reliable prediction of adsorption isotherms via genetic algorithm molecular simulation. *J. Mol. Model.* 2017, 23(1):33.